INTERCALATION OF GRAPHITE WITH MICROCLUSTER WATER IN ULTRASONIC AND MAGNETIC FIELD

Yurov V.,
Candidate of Physics and Mathematics Sciences, Associate Professor
KarTU, Karaganda, Kazakhstan
Zhangozin K.,
Candidate of Physics and Mathematics Sciences, Associate Professor,
TSK Vostok LLP, Astana, Republic of Kazakhstan
Kargin D.
Candidate of Physical and Mathematical Sciences, Associate Professor
NAO "L.N. Gumilyov Eurasian National University",
Astana, Kazakhstan
https://doi.org/10.5281/zenodo.15879910

Abstract

The article presents an experimental and theoretical study of natural graphite exfoliation by microcluster water in the presence of ultrasound and a stationary magnetic field. Theoretically, ultrasonic exfoliation of graphite is considered as a Stefan problem for a finite cylinder. It is shown that graphite intercalation will increase in the system +liquid-graphite" with an increase in the ultrasound power and surface tension of the liquid. It is shown that water has the highest surface tension (except mercury) and surpasses all liquids in ultrasonic splitting of graphite in order to obtain graphene plates from it. The effect of ultrasound on graphite splitting is far from complete. Particular attention should be paid to the theory of cavitation and its nonlinearity. It is shown that any effect on water (chemical impurities, ultrasound, magnetic field, etc.) leading to an increase in the surface tension of water will contribute to the exfoliation of graphite. It is shown that the energy of graphite deformation under external influence (ultrasound, friction, magnetic field, etc.) is spent on heat, acoustic emission, autoelectronic emission and fractoluminescence. Due to the law of conservation of energy, the energy of deformation should be comparable with the energy of ultrasound, leading to the stratification of graphite with the formation of grapheme.

Keywords: graphite, graphene, intercalation, ultrasound, magnetic field, delamination, deformation, surface layer

Introduction

Layered graphite crystals were exfoliated mechanically using adhesive tape in 2004 [1]. A single-layer graphite sheet was called graphene. However, it is impossible to use mechanically obtained graphene on an industrial scale. Therefore, various methods for obtaining graphene have appeared, an overview of which is given in [2-5].

The purpose of this article is to study the production of graphene by intercalation of graphite with microcluster water in ultrasound and in a magnetic field using the RIMS complex.

Graphite intercalation in ultrasound (brief overview)

Let us turn to the latest works. Thus, in [6], to prepare the initial mixture, precise weighed components were used: 1 mg of thermally expanded graphite (TEG), 14 mg of a 2% Nafion solution, 4 ml of a mixture of isopropanol + water (1:1) were added. The mixture was subjected to ultrasonic treatment in a Branson 3510 ultrasonic bath at a power of ~ 180 W for ~ 180 min. After that, 2 drops (0.04 ml) were collected from the resulting suspension, 4 ml of an isopropanol + water mixture (1:1) were added, and ultrasonic dispersion was carried out for different durations. The results are shown in Fig. 1.

Fig. 1b shows the Raman spectrum of a dispersed material film obtained by spraying the dispersion with an airbrush onto a silicon wafer. Three most significant clear lines are visible in the Raman spectrum: D, G and 2D, as well as the D′ line. The presence of an intense D line, as well as a D′ line in the Raman spectrum, indicates a fairly high degree of defectiveness of the material. Data on the ratio of the integrated intensities of the D and G lines (AD/AG = 2.1) and the full width at half height of the G line (FWHM(G) = 40 cm^{-1}) make it possible to estimate the concentration of one-dimensional (crystallite boundaries) and 0-dimensional (point) defects in graphene.

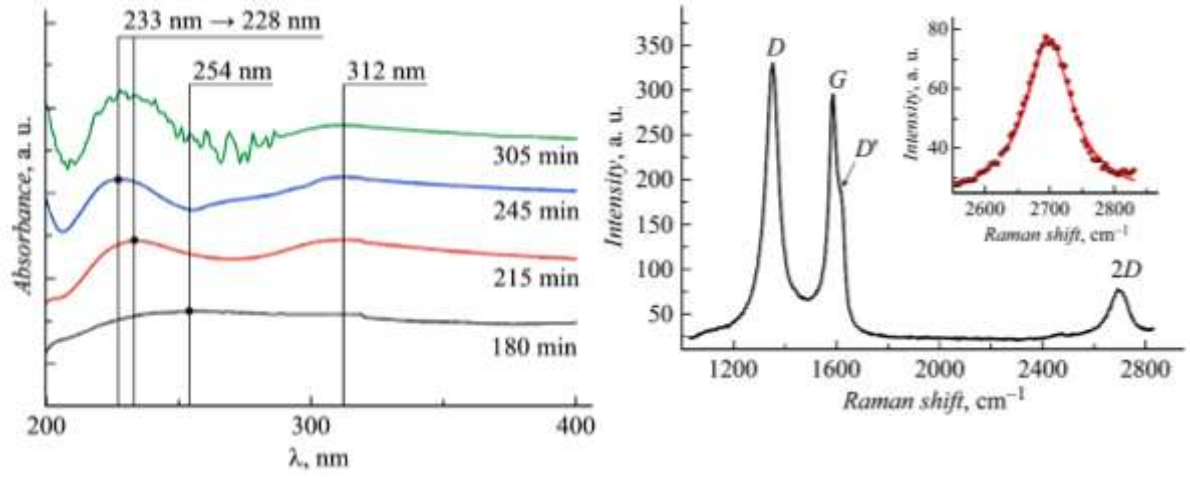

a) *b)*

Figure 1. - UV spectra of the dispersion of TEG-Nafion in a mixture of isopropanol with water (1:1) during dispersion (a); Raman spectrum of the obtained graphene layer (b) [6].

The 2D line is well approximated by a single Lorentz function (insert in Fig. 1b), which is typical for graphene. At the same time, due to the presence of defects in its crystal lattice, the 2D line has a fairly large width (FWHM ~ 90 cm^{-1}), which is typical for graphene with a thickness of about 2-3 monolayers.

In [7], mechanical stirring and ultrasonic (US) treatment are used to separate graphite electrode materials from copper foil during the recycling of spent lithium-ion batteries (LIB). Firstly, the effects of ultrasonic power (60~180W), ultrasonic time (1~8 min), stirring speed (420~2000 rpm) and stirring time (1~8 min) on the separation rate of the active material from the copper foil were studied. It was found that the separation rate of the electrode material in the ultrasonic treatment was 91.34% compared with that in the stirring treatment (84.22%). The removal of the electrode material from the copper foil during stirring was mainly realized by mechanical cleaning. In comparison, the generation of micro jets caused by ultrasound, local high-temperature and high-pressure environment, and free radicals during ultrasonic treatment are the key factors to further improve the removal efficiency of the electrode material. The integrated ultrasonic mechanical stirrer technology can achieve highly efficient separation performance (approximately 100% peeling rate) of the anode electrode materials from the copper foil. The effects of mechanical stirring speed, temperature and treatment time on the peeling coefficients of the ultrasonic mechanical stirrer system were investigated. Finally, the results of XRF (X-ray fluorescence spectrometer), XRD (X-ray diffraction) and SEM-EDS (scanning electron microscopy coupled with energy dispersive X-ray spectroscopy) showed that the graphite electrode material after peeling was of high purity and contained almost no copper foil impurity. The numerical simulation analysis briefly showed that the difference between the pressure and ultrasonic temperature changes at the interface between different anode layers (graphite on copper foil in aqueous solution) was the main effective factor in significantly peeling off graphite from copper anode foil in ultrasonic peeling. The main effect of ultrasonic action on water is cavitation. Acoustic cavitation can cause both isotropic and anisotropic collapse of bubbles in water, resulting in shock waves and microjets (Fig. 2) [7].

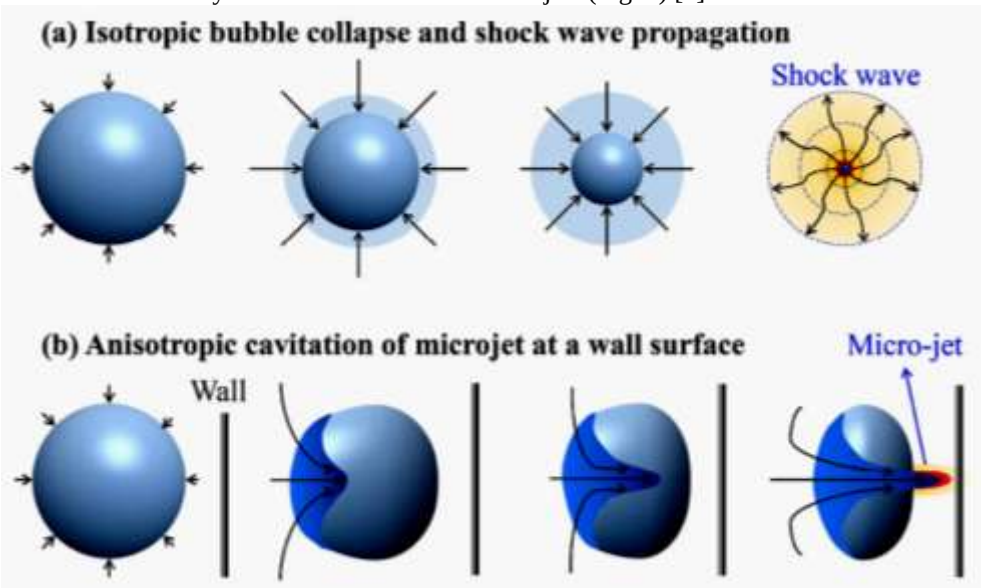

Figure 2.
Schematic diagram of a shock wave (a) and a microjet (b) formed during the collapse of a cavitation bubble [7].

Samples and research methods, RIMS complex

We used natural graphite of the GL-1 brand. Ultrasonic (US) dispersion of natural graphite in the liquid-graphite system was carried out in the Sapphire UZV-5.7 ultrasonic bath (Fig. 3).

Technical characteristics of the ultrasonic bath Sapphire UZV-5.7

Volume	5.7 l
Operating frequency	35 kHz
Timer digital	1-99±1 min
Power consumption	280 W
Thermostat digital	15-65±1 °C
Heater power	130 W
Generator power	150 W
Supply voltage	220 V 50-60 Hz

Figure 3. – Ultrasonic bath "Sapphire UZV-5.7"

To conduct research in a magnetic field, a suspension obtained after ultrasonic dispersion in an ultrasonic bath was used (Fig. 4).

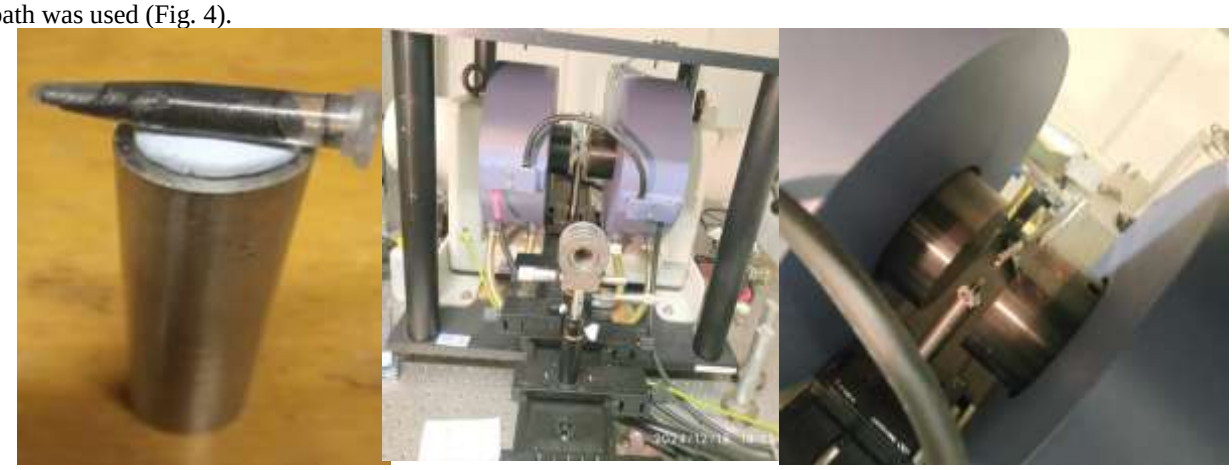

a) *b)*

Figure 4. – Vessel with graphite suspension after MCW (a) magnet (b).

The morphology of the samples was studied by SEM on a JEOL. The accelerating voltage varied from 2 to 20 kV. The method allows one to study the morphology of films, particle sizes and film thickness. X-ray diffraction spectra (FTIR) were obtained on a Brucker D8 Discover (Fig. 5).

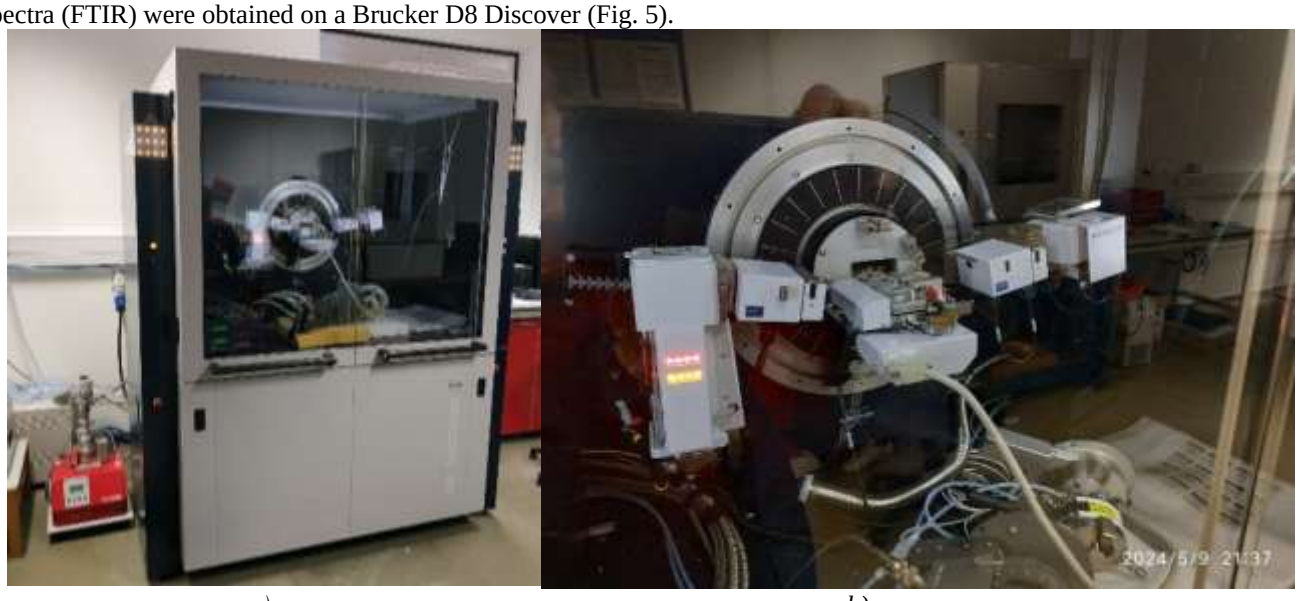

a) *b)*

Figure 5. - Diffractometer (a); its working chamber (b)

Spectroscopic workstation with Raman spectroscopy, basic fluorescence spectroscopy, UV/VIS includes:

a) TEC spectrometer cooled to -40 0C: focal length 200-4000 cm-1; focal length 250 mm, resolution from 1 to 3 cm (-). Detector Raman channel (pre-equipped with 2D-detector)

b) TEC spectrometer cooled to -35 ^{0}C: focal length 200-1100 nm (focal length 120 mm), channel 2 for the RIUS part Detector: Linear CCD array, 3648 pixels Slit: Continuous variable.

Photo of the device is shown in Fig. 6.

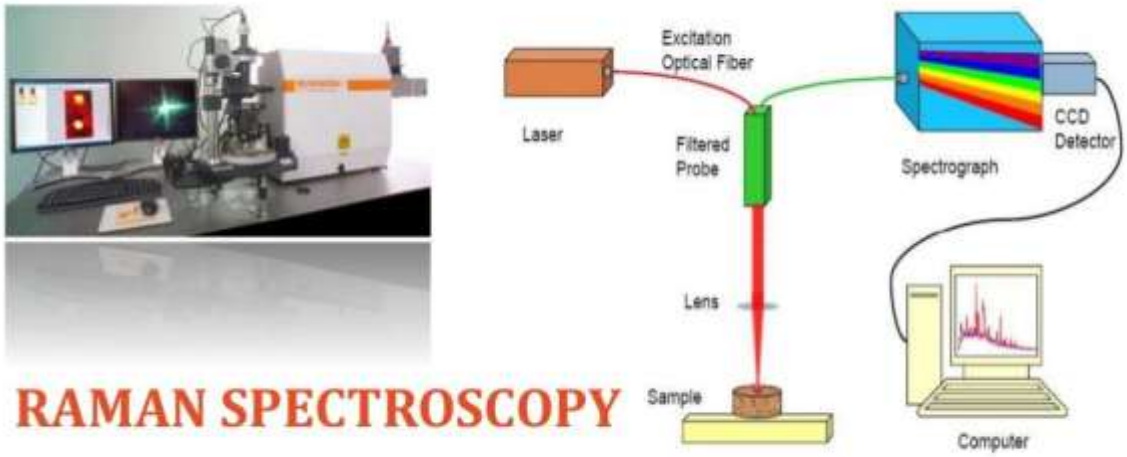

Figure 6. - Spectroscopic workstation

Results of the study

The stratification of MCW graphite during ultrasonic dispersion in an ultrasonic bath is shown in Fig. 7.

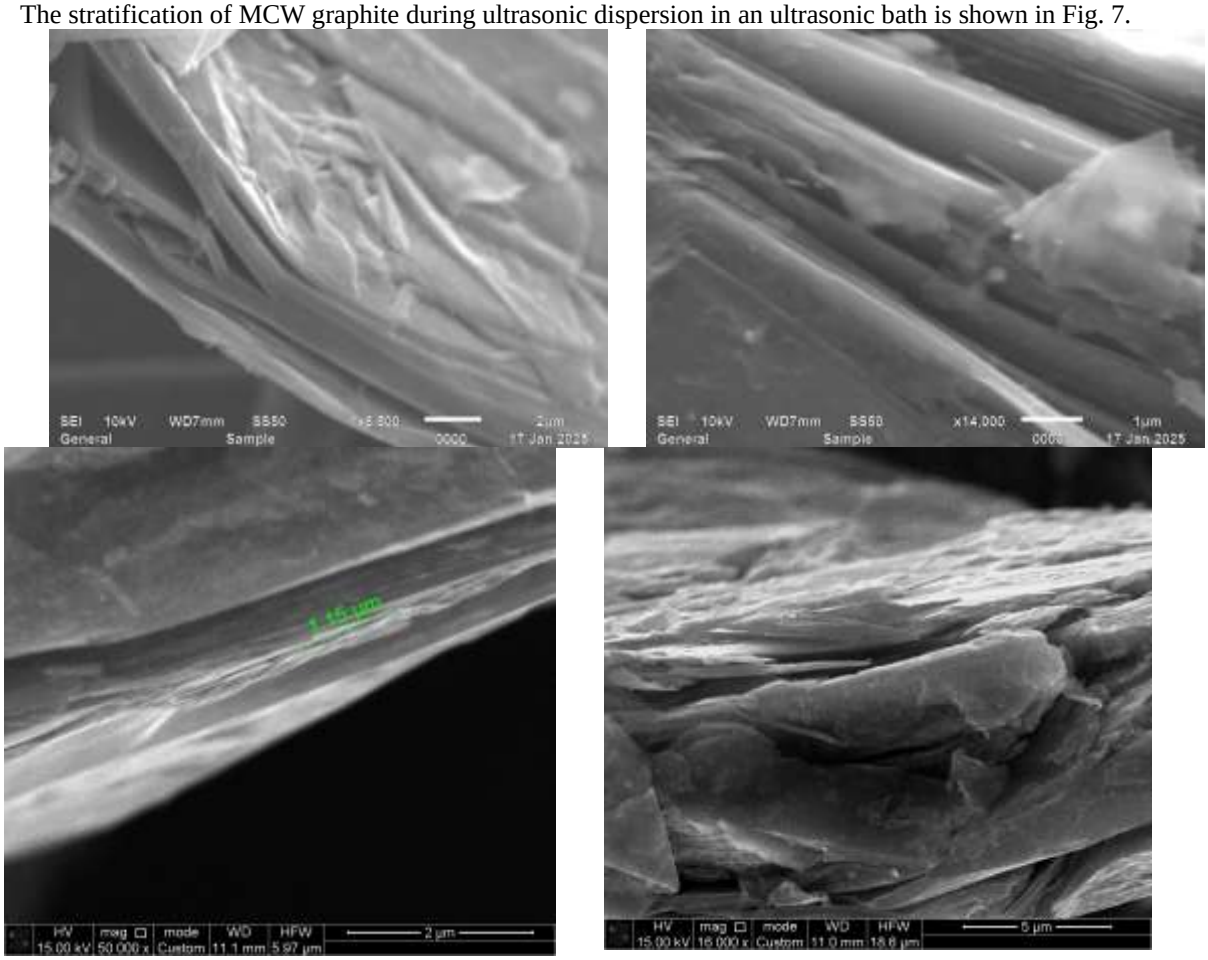

Figure 7. – Exfoliated natural graphite

Comparison of FTIR and XRD spectra for dried graphite solutions in normal/microcluster/distilled water with and without an applied external magnetic field shows that there is a certain correlation between them (Fig. 8) and Table 1.

Table 1.

Values of intensity drop of absorption spectra

	Without magnetic field	With magnetic field	Decrease, in %
MCW	63,24	57,1	10,9
Distilled water	62,45	52,77	18,3
Regular water	72,55	56,98	27,3

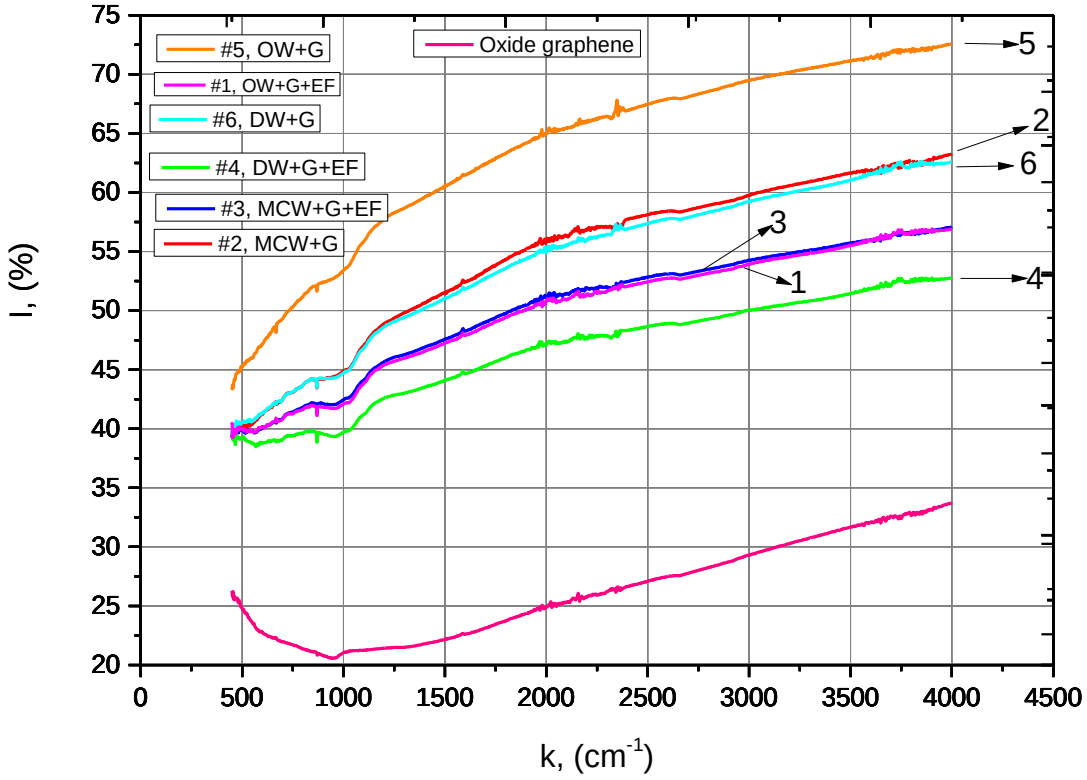

Figure 8. - Absorption spectra at 4000 cm^{-1}

Raman spectra of graphene were measured on the RIMS complex and are shown in Fig. 9. Raman spectroscopy or Raman spectroscopy allows obtaining information on the number of graphene layers by analyzing the "shear" and "breathing" modes that arise due to interlayer interactions in graphite.

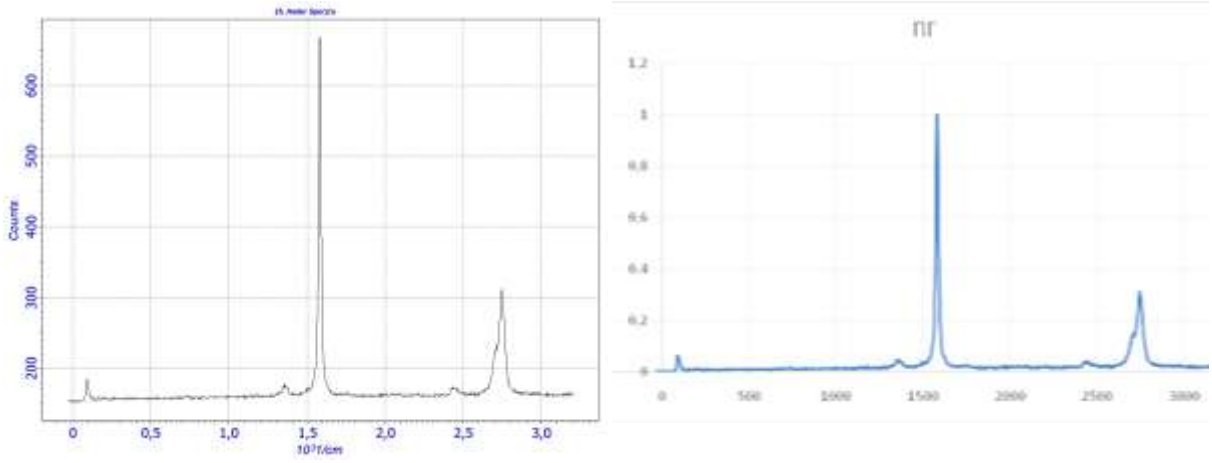

a) *b)*

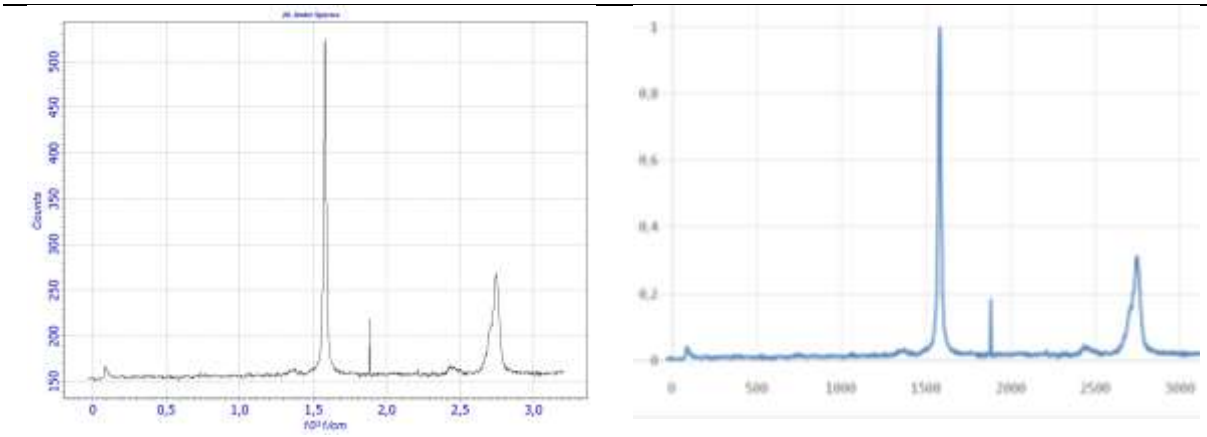

c) *d)*

Figure 9. - Raman spectrum of the original graphite (a); normalized Raman spectrum of the original graphite (b); spectrum of graphite intercalated with MCW in ultrasound (c); normalized spectrum of graphite intercalated with MCW in ultrasound (d).

Discussion of the research results

Graphite is a thermodynamically stable allotropic modification of carbon - an element of the 4th group of the main subgroup of the 2nd period of the periodic table, atomic number 6, the atomic mass of the natural mixture of isotopes is 12.0107 g/mol. The theoretical density of 2.26 g/cm^3 is achieved only in natural graphite. The density of artificial graphite is in the range of 1.65-1.75 g/cm^3. Such a low density of artificial graphite is explained by its porosity [8].

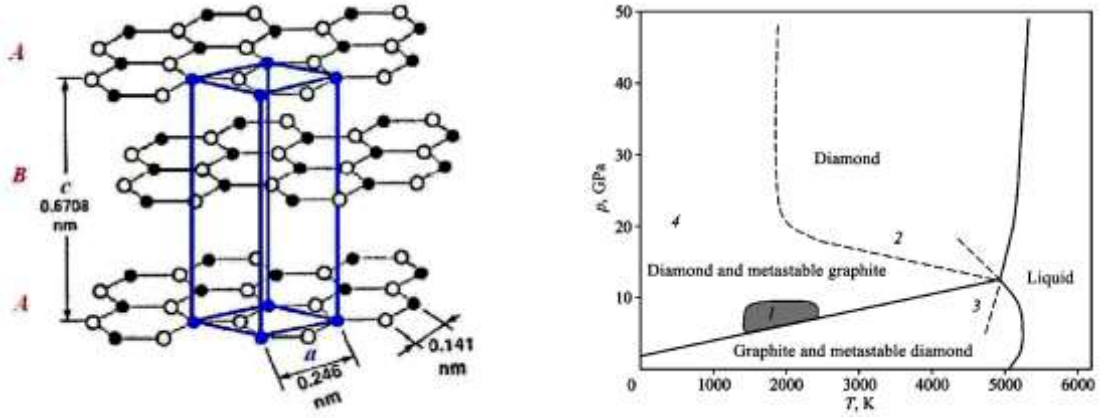

a) *b)*

Figure 10. - Graphite structure (a) [8] and carbon diagram (b) [9].

The crystalline structure of graphite has hexagonal symmetry and consists of flat layers of carbon atoms located parallel to each other (Fig. 10a). The phase diagram of carbon according to Bundy [9] is shown in Fig. 10b.

The thickness of the surface layer R(I) is given by the formula [10]:

$$R(I) = L_{nm} = 0{,}17 \cdot 10^{-9} \cdot \alpha \cdot \upsilon \text{ [m]}. \quad (1)$$

In equation (1) one parameter must be known – the molar volume of the element, which is equal to υ = M/ρ (M is the molar mass, ρ is its density), α = 1 mol m^{-2} is a constant to maintain the dimensionality (R(I) = [m]). The diagram of the surface layer is shown in Fig. 11.

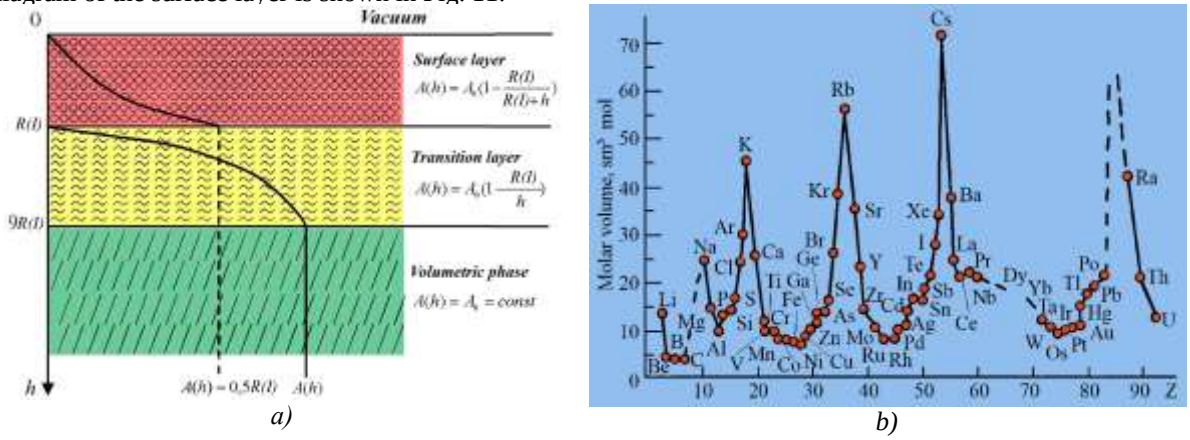

a) *b)*

Figure 11.
Schematic representation of the surface layer (a), periodic change in the atomic volume of elements (b) [10].

Using formula (1), we calculate R(I) (Table 2) for graphite parallel to the plane x = a = b and perpendicular to this plane x = c.

Table 2.

Parameters R(I) of graphite.

Graphite	Structure	M, g/mol	ρ, g/cm^3	R(I)$_a$, nm	R(I)$_c$, nm
C	C6/mmc-D$^4_{6h}$	12,0107	2,26	0.90 (3)	2.46 (3)
			1,75	1.17 (4)	3.19 (4)
			1,65	1.24 (5)	3.39 (5)

From Table 2 it is evident that natural graphite has three (3) graphene monolayers (Fig. 12), which are detected by the Raman method (Fig. 9).

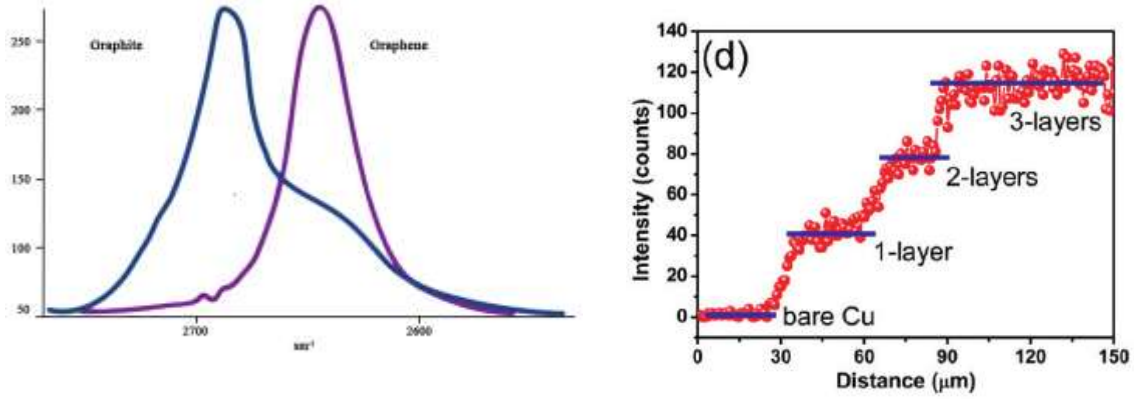

a) *b)*

Figure 12. - 2D Raman band of graphite and graphene (a); number of graphite monolayers (b).

The first monolayer of graphite is graphene, it is determined by the unique physicochemical properties of graphene, such as a large specific surface area (~ 2600 m^2/g), high mobility of charge carriers (~ 200,000 cm^2/V•s), high Young's modulus (~ 1000 GPa), thermal conductivity (~ 5000 W/m K), optical transparency (~ 97.7%), mechanical strength, etc. [11].

Bilayer graphene differs from single-layer graphene and graphite. It is actively studied [12] due to the controllable width of the band gap. An analogue of bilayer graphene is SW graphene, which is more stable than graphene [13].

Three-layer graphene differs from the latter two in mobility and conductivity [14]. A special feature of three-layer graphene is that after its twisting at a magic angle, it develops superconductivity, which can withstand magnetic fields 2-3 times greater than the Pauli limit for spin-singlet pairing [15]. Let us consider the issue of ultrasonic dispersion theoretically as a Stefan problem, using an analytical solution to the non-stationary problem. The non-stationary diffusion equation in a moving cylindrical coordinate system moving according to the law β(t) has the form:

$$\frac{\partial U}{\partial t} = Д\left[\frac{\partial^2 U}{\partial z^2} + \frac{1}{r}\frac{\partial}{\partial r}\left(r\frac{\partial U}{\partial r}\right)\right], \tag{2}$$

where D is the diffusion coefficient.

We will choose the initial and boundary conditions in a general form:

$$U(r, z, t)|_{t=0} = \varphi(r, z), \tag{3}$$

$$U(r, z, t)|_{r=R} = \gamma(z, t), \tag{4}$$

$$U(r, z, t)|_{z=0} = \gamma_1(r, t), \tag{5}$$

$$U(r, z, t)|_{z=\beta(t)} = \gamma_2(r, t). \tag{6}$$

We will consider the functions $\beta(t), \varphi(r,z), \gamma(z,t), \gamma_1(r,t)\, u\, \gamma_2(r,t)$ to be continuous. We seek the solution to the problem in the form:

$$U(r,z,t) = \sum_{k=o}^{\infty} \overline{U}_k(z,t) I_0(\lambda_{0k} r), \tag{7}$$

where λ_{ok} are the roots of the equation

$$I_0(\lambda_{ok} R) = 0 \tag{8}$$

and $I_o(\lambda_{ok}R)$ is the zero-order Bessel function satisfying the equation:

$$\frac{1}{r}\frac{d}{dr}\left[r\frac{dI(\lambda_{0k}r)}{dr}\right]+I_0(\lambda_{0k}r)=0, \tag{9}$$

$$\overline{U}_k(z,t)=\int_0^R U_k(r,z,t)I_0(\lambda_0 r)rdr. \tag{10}$$

Applying the integral transformation (10) and taking into account (7) and (8), we reduce equation (2) to the form:

$$\frac{1}{Д}\frac{\partial\overline{U}_k}{\partial t}=\frac{\partial^2\overline{U}_k}{\partial z^2}+\overline{\Phi}_k(z,t)-\overline{U}_k(z,t), \tag{11}$$

Using the substitution $\overline{U}_k=\widetilde{U}_k e^{-Ät}$ and transforming the boundary conditions in a similar way, we obtain the following problem:

$$\frac{1}{Д}\frac{\partial\widetilde{U}_k}{\partial t}=\frac{\partial^2\widetilde{U}_k}{\partial z^2}+\widetilde{\Phi}_k(z,t), \tag{12}$$

$$\widetilde{U}_k(z,t)|_{t=0}=\widetilde{\varphi}(z), \tag{13}$$

$$\widetilde{U}_k(z,t)|_{z=0}=\widetilde{\gamma}_1(t), \tag{14}$$

$$\widetilde{U}_k(z,t)|_{z=\beta(t)}=\widetilde{\gamma}_2(t), \tag{15}$$

in the area $Д:(t>0,\ 0<z<\beta(t))$.

We seek the solution to problem (12)-(15)) in the form of the sum of potentials of the first and second kind, as well as two double layer potentials:

$$\widetilde{U}_k(z,t)=\frac{1}{2\sqrt{Д}}\int_0^\ell\frac{\widetilde{\varphi}(\xi)}{\sqrt{\pi t}}e^{-\frac{(z-\xi)^2}{4Дt}}d\xi+\int_6^t d\tau\int_0^\ell\frac{\widetilde{\Phi}_k(\xi,\tau)}{2\sqrt{\pi Д(t-\tau)}}e-\frac{(z-\xi)^2}{4Д(t-\tau)}d\xi+$$

$$+\frac{1}{4\sqrt{\pi}}\int_0^t\frac{z}{[Д(t-\tau)]^{3/2}}e^{-\frac{z^2}{4Д(t-\tau)}}K_1(\tau)d\tau+ \tag{16}$$

$$+\frac{1}{4\sqrt{\pi}}\int_0^t\frac{z-\beta(\tau)}{[Д(t-\tau)]^{3/2}}e^{-\frac{[z-\beta(\tau)]^2}{4Д(t-\tau)}}K_2(\tau)d\tau.$$

Using conditions (14), (15), we obtain a system of integral equations:

$$\widetilde{\gamma}_1'(t)=\frac{K_1(t)}{2Д}-\frac{1}{4\sqrt{\pi}}\int_0^t\frac{\beta(\tau)}{[Д(t-\tau)]^{3/2}}e^{-\frac{\beta^2(\tau)}{4Д(t-\tau)}}K_2(\tau)d\tau,$$

$$\widetilde{\gamma}_2'(t)=\frac{K_2(t)}{2Д}+\frac{1}{4\sqrt{\pi}}\int_0^t\frac{\beta(t)-\beta(\tau)}{[Д(t-\tau)]^{3/2}}e^{-\frac{[\beta(t)-\beta(\tau)]^2}{4Д(t-\tau)}}K_2(\tau)d\tau+$$

$$+\frac{1}{4\sqrt{\pi}}\int_0^t\frac{\beta(t)}{[Д(t-\tau)]^{3/2}}e^{-\frac{\beta^2(t)}{4Д(t-\tau)}}K_1(\tau)d\tau \tag{17}$$

where $\widetilde{\gamma}_1'(t)=\widetilde{\gamma}_1(t)-\frac{1}{2}\int_0^\ell\frac{\widetilde{\varphi}(\xi)}{\sqrt{\pi Дt}}e^{-\frac{\xi^2}{4Дt}}d\xi-\int_0^t d\tau\int_0^\ell\frac{\widetilde{\Phi}_k(\xi,\tau)}{2\sqrt{\pi Д(t-\tau)}}\cdot e^{-\frac{\xi^2}{4Д(t-\tau)}}d\xi$;

$$\widetilde{\gamma}_2'(t)=\widetilde{\gamma}_2(t)-\frac{1}{2}\int_0^\ell\frac{\widetilde{\varphi}(\xi)}{\sqrt{\pi Дt}}e^{-\frac{[\beta(t)-\xi]^2}{4Дt}}d\xi-\int_0^t d\tau\int_0^\ell\frac{\widetilde{\Phi}_k(\xi,\tau)}{2\sqrt{\pi Д(t-\tau)}}\cdot e^{-\frac{[\beta(t)-\xi]^2}{4Д(t-\tau)}}d\xi.$$

Eliminating from the first equation of system (17) and substituting into the next equation $K_t(t)$, we have:

$$\tilde{\gamma}_2'(t)=\frac{K_2(t)}{2Д}+\frac{1}{4\sqrt{\pi}}\int_0^t\frac{\beta(t)-\beta(\tau)}{\left[Д(t-\tau)\right]^{3/2}}e^{-\frac{[\beta(t)-\beta(\tau)]^2}{4Д(t-\tau)}}K_2(\tau)d\tau+$$

$$+\frac{2Д}{\sqrt{\pi}}\int_0^t\frac{\beta(t)}{\left[Д(t-\tau)\right]^{3/2}}e^{-\frac{\beta^2(t)}{4Д(t-\tau)}}\tilde{\gamma}_1'(\tau)d\tau+ \tag{18}$$

$$+\frac{Д}{8\pi}\int_0^t\frac{\beta(t)}{\left[Д(t-\tau)\right]^{3/2}}e^{-\frac{\beta^2(t)}{4Д(t-\tau)}}\left(\int_0^\tau\frac{\beta(\tau_1)}{\left[Д(t-\tau_1)\right]^{3/2}}e^{-\frac{\beta^2(t)}{4Д(t-\tau)}}K_2(\tau_1)d\tau_1\right)d\tau.$$

Introducing the notation

$$q(t)=\tilde{\gamma}_2(t)-\frac{Д}{2\sqrt{\pi}}\int_0^t\frac{\beta(t)}{\left[Д(t-\tau)\right]^{3/2}}\tilde{\gamma}_1'(\tau)e^{-\frac{\beta^2(t)}{4Д(t-\tau)}}d\tau, \tag{19}$$

and calculating the integral in (18), we obtain

$$-\frac{K_2(t)}{2Д}+\frac{1}{4\sqrt{\pi}}\int_0^t\frac{\beta(t)-\beta(\tau)}{\left[Д(t-\tau)\right]^{3/2}}e^{-\frac{[\beta(t)-\beta(\tau)]^2}{4Д(t-\tau)}}K_2(\tau)d\tau+$$

$$+\frac{1}{4\sqrt{\pi}}\int_0^t\frac{\beta(t)}{\left[Д(t-\tau)\right]^{3/2}}e^{-\frac{\beta(t)^2}{4Д(t-\tau)}}K_2(\tau)d\tau=q(t). \tag{20}$$

Designating,

$$\lambda=\frac{1}{2\sqrt{Д}},\quad f(t)=2Дq(t),\ K(t,\tau)=\frac{\lambda}{\sqrt{\pi}}\frac{\beta(t)-\beta(\tau)}{(t-\tau)^{3/2}}\,x$$

$$x\,e^{-\lambda^2\frac{[\beta(t)-\beta(\tau)]^2}{(t-\tau)}}+\frac{\lambda}{\sqrt{\pi}}\frac{\beta(t)}{(t-\tau)^{3/2}}e^{-\lambda^2\frac{\beta(t)^2}{(t-\tau)}}, \tag{21}$$

we obtain the integral equation

$$K_2(t)-\int_0^t K(t,\tau)\,K_2(t,\tau)\,d\tau=f(t). \tag{22}$$

The integral equation (22) is Volterra in C(0,l) if and only if:

$$\lim_{t\to 0}\int_0^t K(t,\tau)d\tau=0.$$

Indeed, given that $e^{-z}<1$ for $z>0$, it is easy to show that the above equality holds. Then for equation (22) there is a unique solution, which has the form:

$$K_2(t)=\sum_{n=0}^{\infty}K_{2,n}(t), \tag{23}$$

$$K_{2,0}(t)=f(t),$$

$$K_{2,1}(t)=\int_0^t K(t,\tau)\,K_{2,0}(\tau)d\tau,$$

$$K_{2,2}(t)=\int_0^t K(t,\tau)\,K_{2,1}(\tau)d\tau,$$

……

$$K_{2,n}(t)=\int_0^t K(t,\tau)\,K_{2,n-1}(\tau)d\tau$$

……..

and (23) converges absolutely and uniformly in the topology C(0,l).

Then

$$K_1(t)=2Д\tilde{\gamma}_1(t)+\frac{Д}{2\sqrt{\pi}}\int_0^t\frac{\beta(t)}{\left[Д(t-\tau)\right]^{3/2}}e^{-\frac{\beta^2(\tau)}{4Д(t-\tau)}}\sum_{n=0}^{\infty}K_{2,n}(\tau)d\tau. \tag{24}$$

Performing the inverse transformation, we finally have:

$$U(r,z,t)=\sum_{\kappa=0}^{\infty}J_0(\lambda_{o\kappa}r)\left\{e^{-Дt}\left[\frac{1}{2Д\sqrt{\pi}}\int_0^t e^{\frac{(z-\xi)^2}{4Дt}}dt\,x\right.\right.$$

$$x\left(\int_0^{\ell}\varphi(r,\xi)I_0(\lambda_{ok}r)rdr\right)d\xi+\frac{RI_1(\lambda_{ok}R)}{2\sqrt{\pi}Д}\int_0^t d\tau\int_0^{\ell}\frac{\gamma(\xi,\tau)}{\sqrt{t-\tau}}e^{-Дt}e^{-\frac{(z-\xi)^2}{4Д(t-\tau)}}d\xi+$$

.

$$\left.\left.+\frac{1}{4\sqrt{\pi}}\int_0^t\frac{z}{[Д(t-\tau)]^{3/2}}e^{-\frac{z^2}{4Д(t-\tau)}}K_1(\tau)d\tau+\frac{1}{4\sqrt{\pi}}\int_0^t\frac{z-\beta(\tau)}{[Д(t-\tau)]^{3/2}}e^{-\frac{[z-\beta(\tau)]^2}{4Д(t-\tau)}}K_2(\tau)d\tau\right]\right\}. \quad (25)$$

Thus, an analytical solution to the problem of crystallization of a cylinder of finite dimensions is obtained.

Let us choose the boundary conditions in the simplest periodic form. The diffusion problem in this case has the boundary conditions:

$$\begin{aligned}
&\frac{\partial C}{\partial t}=Д\left[\frac{\partial^2 C}{\partial z^2}+\frac{1}{r}\frac{\partial}{\partial r}\left(r\frac{\partial C}{\partial r}\right)\right]\\
&C(r,z,t)\big/_{t=0}=\varphi(r,z)\\
&C(r,z,t)\big/_{t=R}=\gamma(z,t)=C_0\sin\omega t\sin\boldsymbol{\kappa r},\\
&C(r,z,t)\big/_{z=0}=\gamma_1(r,t)=C_1\sin\omega t\sin\boldsymbol{\kappa r},\\
&C(r,z,t)\big/_{z=\beta(t)}=\gamma_2(r,t)=C_2\sin\omega t\sin\boldsymbol{\kappa r}.
\end{aligned} \quad (26)$$

where C_0, C_1, C_2 are the concentration of the substance on the side walls of the crystallizer and on the moving phase boundary, respectively; ω, k are the cyclic frequency of the disturbing field and the wave vector.

The general solution to such a problem is given above:

$$C(r,z,t)=\sum_{\kappa=0}^{\infty}J_0(\lambda_{o\kappa}r)\left\{e^{Дt}\left[\frac{1}{2\sqrt{Д\pi}}\int_0^t e^{\frac{(z-\xi)^2}{4Дt}}dt\,x\right.\right.$$

$$x\left(\int_0^{\ell}\varphi(r,\xi)I_0(\lambda_{ok}r)rdr\right)d\xi+\frac{RI_1(\lambda_{ok}R)}{2\sqrt{Д\pi}}\int_0^t d\tau\int_0^{\ell}\frac{\gamma(\xi,\tau)}{\sqrt{t-\tau}}e^{-Дt}e^{-\frac{(z-\xi)^2}{4Д(t-\tau)}}d\xi+$$

$$\left.\left.+\frac{1}{4\sqrt{\pi}}\int_0^t\frac{z}{[Д(t-\tau)]^{3/2}}e^{-\frac{z^2}{4Д(t-\tau)}}K_1(\tau)d\tau+\frac{1}{4\sqrt{\pi}}\int_0^t\frac{z-\beta(\tau)}{[Д(t-\tau)]^{3/2}}e^{-\frac{[z-\beta(\tau)]^2}{4Д(t-\tau)}}K_2(\tau)d\tau\right]\right\}. \quad (27)$$

On the z-axis and at r=0, we have

$$C(z,t)=\frac{1}{4\sqrt{\pi}}\left(\int_0^t\frac{z}{[Д(t-\tau)]^{\frac{3}{2}}}e^{-\frac{z^2}{4Д(t-\tau)}}K_1(\tau)d\tau+\int_0^t\frac{z-\beta(\tau)}{[Д(t-\tau)]^{\frac{3}{2}}}e^{-\frac{[z-\beta(\tau)]^2}{4Д(t-\tau)}}K_2(\tau)\right)d\tau. \quad (28)$$

Taking β(τ) = H (i.e. for a finite cylinder of depth H and radius R), calculating $K_1(\tau)$ and $K_2(\tau)$, for the axial concentration gradient we have:

$$\partial C/\partial z=\frac{8\pi\upsilon}{\lambda}\cdot\sqrt{\frac{\pi}{Д}}e^{-\frac{(z-h)^2}{4Д}t}(C_1+C_2). \quad (29)$$

where υ, λ are the speed and wavelength of the alternating field; h is the distance to the horizontal plane coinciding with the cross-section of the source of the excited field.

Let us designate:

$$W=\frac{8\pi\upsilon}{\lambda}\cdot\sqrt{\frac{\pi}{Д}}(C_1+C_2). \quad (30)$$

Finally, we can write down:

$$\partial C/\partial z=W\cdot e^{-\frac{(z-h)^2}{4Д}t}. \quad (31)$$

From formula (31) it follows that the presence of periodic boundary conditions simulating periodic ultrasonic action on the "water-graphite" system leads to an exponential law of change in the vertical component of concentration, where:

$$\upsilon = \frac{\omega\lambda}{2\pi} \tag{32}$$

In other words, graphite intercalation will increase in the system + liquid-graphite" with an increase in the ultrasound power ~ υ and the surface tension of the liquid ~ γ. According to the classical theory, D = ν, where ν is the kinematic coefficient of viscosity. We have shown that ν ~ 1/γ and therefore W ~ $\gamma^{1/2}$.

Let us present some values of γ for some liquids.

Table 3.

Surface tension of liquids at 20 ºC [16]

Liquid	γ, 10^{-3} N/m	Liquid	γ, 10^{-3} N/m	Liquid	γ, 10^{-3} N/m
water	72,75	glycerol	63,40	chloroform	27,14
acetonitrile	26,64	phenol	40,90	benzene	28,88
toluene	28,40	acetone	23,70	ethyl acetate	23,60
orthoxylene	30,10	ethanol	22,80	mercury	465,0

It follows from Table 3 that water has the highest γ value (except mercury) and surpasses all liquids in the ultrasonic splitting of graphite to obtain graphene plates from it. The effect of ultrasound on the splitting of graphite is far from complete. Particular attention should be paid to the theory of cavitation and its nonlinearity. The splitting of graphite is the destruction of solids, where it is necessary to apply the theory of catastrophes. When graphite is split, many new planes arise that differ significantly from the properties of bulk graphite. This list can be continued, but the main thing is to obtain graphene plates or flakes suitable for their practical application.

Intercalation of water into graphite and its subsequent stratification is possible when the following relationships are met:

$$\begin{aligned} W(C) - W(H_2O) &\to \min, \\ \gamma(C) - \gamma(H_2O) &\to \min, \end{aligned} \tag{33}$$

where γ(C) = 0.798 J/m^2 is the surface energy of graphite in the c plane; γ(H_2O) = 0.0728 J/m^2 is the surface energy (surface tension) of water.

Equation (33) shows that any impact on water (chemical impurities, vibration, ultrasound, electric and magnetic fields, increased temperature, etc.) leading to an increase in γ(H2O) will contribute to the stratification of graphite.

In the work [15] a system of permanent magnets mounted on a piezoelectric plate was used to activate water to modulate the magnetic field. The conductivity and permittivity of water activated by this source were experimentally studied. The effect of a magnetic field on bidistilled water (0.84 10^{-4} Ohm^{-1}m^{-1}) leads to an increase in surface tension with an increase in the magnitude of the field (Table 4).

Table 4.

Parameters of bidistillate in a magnetic field [17]

Magnetic field, T	pH		Surface tension		Dielectric constant	
	fractions of a unit	%	10^{-3} N/m	%	F/m	%
0.19	0.35	5.1	1.6	2.2	1.5	1.8
0.35	0.44	6.4	3.7	5.1	1.4	1.7
0.48	0.62	9.1	4.7	6.4	1.4	1.7
0.57	0.62	9.1	5.3	7.3	1.4	1.7

From Table 4 it is evident that γ(H_2O) increases with a threefold change in the magnetic field strength, i.e. linearly: γ(H_2O) = α H, where α is the proportionality coefficient, H is the magnetic field strength. Since in our case α = 3, equation (33) yields: γ(C) – 3H = 0 and H ≈ 0.3 T. With such a magnetic field strength, graphite can be exfoliated with water. Graphene, created 21 years ago, is a unique material destined to become the substance of the 21st century. Graphene has a wide range of applications. The global graphene market began to grow only five years ago, which was due to the high cost of graphene. Our proposed method for obtaining graphene from graphite with microcluster water using ultrasound and a magnetic field deserves further study, since it can provide an environmentally friendly and reliable method for obtaining a high-volume initial product.

Thus, using equations (1) - (33) it is possible to obtain exfoliation of graphite with water in a magnetic field and obtain graphene in an environmentally friendly way.

Ultrasonic dispersion

Let us propose another model of ultrasonic dispersion. The nanolayer R(I) of graphite from equation (1) is subject to reconstruction of its surface [18]. In this regard, internal stresses σ_{is} arise at the interphase boundary:

$$\sigma_{is} = \sqrt{W_a \cdot E / R(I)}, \tag{34}$$

where E is Young's modulus.

These stresses lead to deformation, the "latent" energy of which is equal to E_d:

$$E_d = W_a \cdot a^2, \quad (35)$$

where a is the lattice constant.

Above we used the term - "latent" deformation energy, equal to $E_d = W_a a^2$. We took this term from the article [19], where it is shown that the "latent" deformation energy can be represented as a logistic function, characteristic of the theory of catastrophes. The elastic constants are shown in Table 5.

Table 5.

Elastic constants along various planes (a=b, z=c)

Mineral	W_{aa}, J/m^2	W_{ac}, J/m^2	σ_{isa}, GPa	σ_{isc}, GPa	E_{da}, eV	E_{dc} eV
Graphite	2,85	1,69	4,9	1,4	1,08	4,75
Graphene	3,45	-	118,4	-	1,30	-

In [20], we showed that the energy of deformation under external influence (ultrasound, friction, magnetic field, etc.) is spent on heat, acoustic emission, field emission, and fractoluminescence.

First, let us consider the transformation of deformation energy into acoustic emission. Today, several sources of acoustic emission of metals and semiconductors are known: movement of dislocations; initiation and growth of cracks; twinning process [21]. The authors of this article add to this list – the transformation of deformation energy into acoustic emission.

The essence of acoustic emission (AE) consists in the analysis of the parameters of extremely weak ultrasonic radiation accompanying any change in the structure of a solid body, especially during its deformation (Fig. 13).

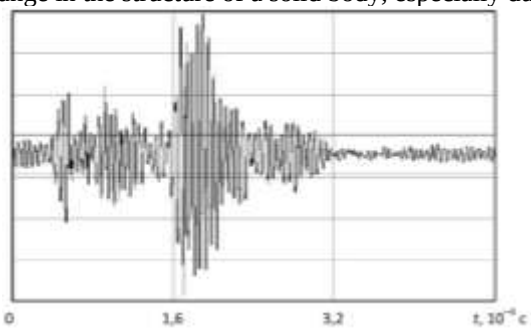

Figure 13. - Typical picture of the fine structure (oscillations) of acoustic emission signals recorded by a sensor on the body surface [22].

The total energy of AE EAE is equal to [23]:

$$E_{AE} = \frac{\sigma_0^2 \cdot \lambda \cdot [R(I)]^2}{8\rho \cdot \upsilon^2}, \quad (36)$$

where σ_0 is (in our case $\sigma_0 \approx \sigma_{is}$) the maximum amplitude of elastic vibration stress; λ is the vibration wavelength (in our case $\lambda = R(I)$; ρ is the density of the body; υ is the speed of sound.

The maximum value of the wavelength λ propagating in a discrete chain of the z axis is equal to $R(I)_c$. The speed of sound in the surface layer of graphite is equal to $\upsilon = R(I)/\tau$, where τ is the relaxation time, which we estimated using the formula from [24]. For longitudinal modes, the time $\tau_L = 0.2\ 10^{-12}$ s, for transverse modes - $\tau_L = 2\ 10^{-12}$ s. For graphite, the speed of sound is shown in Table 6.

Table 6.

Speed of sound modes in graphite and graphene

Graphite	υ_L, m/s	υ_T, m/s
ρ = 2260, kg/m^3	4500	2380
ρ = 1986, kg/m^3 [AE]	3505	1854
ρ = 1753, kg/m^3 [AE]	2631	1591
Graphene	υ_L, m/s	υ_T, m/s
ρ = 0,77, mg/m^2 [AE]	19700	10700

From Table 6 it is evident that graphene has a lower density of matter than graphite, but the speed of sound in it is almost 5 times greater than that of graphite.

Transforming formula (36), we obtain as a result:

$$E_{AE} = \beta \cdot \frac{T_m \cdot E \cdot R(I)}{M} \ (eV), \quad (37)$$

where β = 2 eV kg/K Pa m = const; Tm is the melting point of the solid (K); E is Young's modulus (GPa); M is the mass of the crystal (kg).

Let us estimate E_{AE} for graphite: T_m = 3890 K, E = 3.48 10^9 Pa, R(I) = 2.46 10^{-9} m, M = 12000 kg; then E_{AE} = 4.6 eV. Comparing this value with Table 5, we obtain that $E_{AE} \approx E_{dc}$ = (4.6-4.7) eV and the deformation energy E_d of graphite, arising due to the reconstruction of their surface, coincides within the experimental error with the acoustic emission energy E_{AE}, i.e. $E_d \approx E_{AE}$.

Thus, it can be considered proven that in natural graphite (as in all solids) acoustic emission occurs due to the reconstruction of its surface, leading to the formation of a surface layer R(I) and energy E_d.

Due to the law of conservation of energy, the energy of deformation E_d should be comparable with the energy of ultrasound, leading to the exfoliation of graphite with the formation of graphene.

Conclusion

As a result of experimental and theoretical studies, the following patterns were revealed:

1) Exfoliation of layered graphite crystals was carried out by microcluster water using ultrasound in a magnetic field;

2) It was theoretically shown that any impact on water (chemical impurities, vibration, ultrasound, electric and magnetic fields, increased temperature, etc.) leading to an increase in γ (H_2O) will contribute to the exfoliation of graphite;

3) It was shown that it is possible to obtain exfoliation of graphite with water in a magnetic field and obtain graphene in an environmentally friendly way;

4) A model was proposed: the energy of deformation E_d should be comparable with the energy of ultrasound, leading to the exfoliation of graphite with the formation of graphene.

This scientific article was published within the framework of the grant funding for 2024-2026 IRN No. AR32488258 "Development of an innovative technology for obtaining graphene by intercalation of graphite with microcluster water and modification of HTSC ceramics with graphene" (the research is funded by the Science Committee of the Ministry of Science and Higher Education of the Republic of Kazakhstan).

References:

1. Novoselov, K.S.; Geim, A.K.; Morozov, S.V.; Jiang, D.; Zhang, Y.; Dubonos, S.V.; Grigorieva, I.V.; Firsov, A.A. Electric Field Effect in Atomically Thin Carbon Films // Science, 2004, Vol. 306. – P. 666-669.

2. Zhang T. Graphene. From Theory to Applications. - Springer, ,2022. - 142 p.

3. Zhangozin K.N. New method for producing graphene by intercalation of graphite with microcluster water. - Almaty: Darkhan, 2023. – 102 p.

4. Yurov V., Zhangozin K. About the mechanism of graphite splitting // International independent scientific journal, 2024, №58. – P. 29-40.

5. Yurov V.M., Zhangozin K.N. At the mechanism of graphite splitting bouby aqueous solutions // Znanstvena misel journal, 2024, №86. – P. 41-49.

6. Kastsova A.G., Glebova N.V., Nechitailov A.A., Krasnova A.O., Pelageikina A.O., Eliseev I.A. Electron spectroscopy of graphene obtained by ultrasonic dispersion // Letters to the Journal of Technical Physics, 2022, vol. 48, issue 24. – P. 23-25.

7. Ren X., Tong Z., Dai Y., Ma G., Lv Z., Bu X., Bilal M., Vakylabad A.B., Hassanzadeh A. Effects of Mechanical Stirring and Ultrasound Treatment on the Separation of Graphite Electrode Materials from Copper Foils of Spent LIBs: A Comparative Study // Separations, 2023, Vol. 10. 246.

8. Zhmurikov E.I., Bubnenkov I.A., Dremov V.V., Samarin S.I., Pokrovsky A.S., Kharkov D.V. Graphite in science and nuclear engineering. – Novosibirsk, 2013. – 193 p.

9. Bundy F.P., Bassett W.A., Weathers M.S., et al. The Pressure-Temperature Phase and Transformation Diagram for Carbon; Updated Through 1994 // Carbon, 1996, V. 34, N 2. - P. 141-153.

10. Yurov V.M. Surface layer thickness of atomically smooth crystals // Physicochemical aspects of studying clusters, nanostructures and nanomaterials. - 2019. - issue. 11. - P. 389-397.

11. Novoselov K.S. Graphene: materials of Flatland // Uspekhi fizicheskikh nauk, 2011, Vol. 181, No. 12. - P. 1299-1311.

12. Rozhkov A.V., Sboychakov A.O., Rakhmanov A.L., Noria F. Electronic properties of graphene-based bilayer systems // Physics Reports, 2016, Vol. 648, №1. – P. 1-104.

13. Podlivaev A.I. Bilayer graphene - Stone-Wales graphene: structure, stability and interlayer thermal conductivity // Letters to JETP, 2022, Vol. 115, No. 6. - P. 384-391.

14. Craciun M.F., Russo S., Yamamoto M., Oostinga J.B., Morpurgo A.F. and Tarucha S. Trilayer graphene is a semimetal with a gate-tunable band overlap // Nature Nanotechnology, 2009, Vol. 4. – P. 383-388.

15. Devakul T., Ledwith P.J., Xia L.-Q., Uri A., de la Barrera S., Jarillo-Herrero P., and Fu L. Magic-angle helical trilayer graphene// Science Advances, 2023, Vol. 9 (36): eadi6063.

16. Strelkov S.P. Mechanics. - St. Petersburg: Lan, 2005. - 560 p.

17. Vysotsky V.I., Kornilova A.A. Physical bases of long-term memory of water // Bulletin of Moscow State University, 2004, No. 3. – P.58-62.

18. Yurov V.M., Zhangozin K.N., Kargin D.B. Number of graphene layers in natural graphite // The scientific heritage, 2024, No 143. – P. 75-80.

19. Arutyunyan A.R., Arutyunyan R.A. Formulation of a fatigue criterion based on the concept of latent deformation energy // Physical mesomechanics, 2010, Vol. 13, No. 2. – P. 31-39.

20. Yurov V.M., Goncharenko V.I., Oleshko V.S., Zhangozin K.N. Open quantum system of the surface layer of atomically smooth metals // Journal of Applied and Fundamental Sciences, 2025, No. 4. - P. 52-57.

21. Materials and Acoustics Handbook, Edited by Michel Bruneau Catherine Potel. - ISTE Ltd, 2009. – 919 p.

22. Chernov D.V. Development of methods for diagnosing fatigue cracks using acoustic emission. - Dissertation of candidate of technical sciences, Moscow, 2018. - 148 p.

23. Boyko E.V. Thermoacoustics of graphene coatings and the influence of graphene coating on heat transfer. - Dissertation. candidate of physical and mathematical sciences, Novosibirsk, 2024. - 101 p.

24. Grigoriev E.V. Justification of the method for monitoring the influence of strengthening treatments of welded joints based on the results of recording acoustic emission signals. - Dissertation of Candidate of Technical Sciences, St. Petersburg, 2024. 131 p.